



Trajectory optimization for few-view robot-based CT: Transitioning from static to object-specific acquisition geometries

Maximilian Linde^{a,b,*}, Wolfram Wiest^b, Anna Trauth^{a,1} , Markus G.R. Sause^{a,2} 

^a University of Augsburg, Institute of Materials Resource Management, Am Technologiezentrum 8, Augsburg 86159, Germany

^b Dr. Ing. h.c. F. Porsche AG, Porscheplatz 1, Stuttgart 70435, Germany

ARTICLE INFO

Keywords:

Industrial computed tomography
Robot-based computed tomography
Trajectory optimization
Few-view computed tomography
Limited accessibility

ABSTRACT

The advent of robot-based computed tomography systems accelerated the development of trajectory optimization methodologies, with the objective of achieving superior image quality compared to standard trajectories while maintaining the same or even fewer number of required projections. The application of standard trajectories is not only inefficient due to the lack of integration of available prior knowledge about the object under investigation but also suboptimal because of limited accessibility issues during scans of large components, which are common in robot-based computed tomography. In this work, we introduce an object-specific trajectory optimization technique for few-view applications, based on a 3D Radon space analysis using a RANSAC algorithm. In contrast to existing methods, this approach allows for object geometry specific projection views, which are no longer constrained by discretized initial view sets on predefined acquisition geometries. In addition to eliminating the effects of discretized initial sets, this technique offers a distinct advantage in scenarios of limited accessibility by enabling the avoidance of collision elements, unlike trajectory optimizations on predefined acquisition geometries and standard trajectories. Our results show that the presented technology outperforms standard trajectories of evenly distributed projection views on predefined geometries in both ideal accessibility and limited accessibility scenarios. According to the employed geometry-based image quality metrics, our approach allows for reductions of more than 50 % in the number of projection views while maintaining equivalent image quality.

1. Introduction

Computed tomography (CT) is a popular non-destructive testing (NDT) method in the automotive industry [1]. High-resolution scans in areas of large components, unfeasible in conventional systems due to restricted scanning space of the X-ray cabinets, can be facilitated by the utilization of robot-based computed tomography (RCT) [2,3]. The typical setup employs two cooperating industrial robots equipped with X-ray hardware as end effectors, enabling the implementation of versatile imaging trajectories [4].

In practice, RCT scans frequently encounter situations in scans of large structural components where standard trajectories such as the circular trajectory or the helical trajectory cannot be fully executed due to constraints such as trajectory-limiting elements, singularities, or the

finite workspace of the robots. As a consequence, reconstructed images can exhibit significant artifacts [3]. In addition to the potential loss of information due to accessibility restrictions, conventional trajectories employed in real-world RCT applications neglect to consider that the object under investigation consists of diverse, often metallic materials and may be situated in suboptimal spatial orientations within the inspection region, which can favor the formation of metal artifacts [5].

Due to the limitations of standard trajectories and the high flexibility available in RCT, trajectory optimization for the acquisition process represents a highly compelling area of research.

It has been demonstrated that the information content varies among projection views [6]. Therefore employing the projection views with the highest information content is considered a robust optimization strategy [7]. Especially for recurring inspection tasks and few-view scenarios,

* Corresponding author at: Dr. Ing. h.c. F. Porsche AG, Porscheplatz 1, Stuttgart 70435, Germany

E-mail addresses: maximilian.linde1@porsche.de (M. Linde), wolfram.wiest1@porsche.de (W. Wiest), anna.trauth@uni-a.de (A. Trauth), markus.sause@uni-a.de (M.G.R. Sause).

¹ 0000-0002-3164-4357

² 0000-0002-6477-0691

<https://doi.org/10.1016/j.tmater.2025.100058>

Received 2 December 2024; Received in revised form 14 February 2025; Accepted 26 February 2025

Available online 1 March 2025

2949-673X/© 2025 The Author(s). Published by Elsevier B.V. This is an open access article under the CC BY-NC-ND license (<http://creativecommons.org/licenses/by-nc-nd/4.0/>).

like production-oriented assembly analysis, significant quality improvements can be achieved compared to the utilization of standard trajectories while using a constant or even a reduced number of projections. Reducing the number of projections required for CT examinations allows for at-line and in-line CT inspections of specific regions within large components for quality assurance, despite the short cycle times in automotive production. Thus, geometric analyses such as nominal-actual comparisons, gap analyses, or component positioning can be effectively investigated. Trajectory optimizations that focus on imaging of a particular configuration or geometry, often prioritizing the tangential scanning of edges within the volume, are referred to as task-specific trajectory optimization methods in the literature [5,8,9]. The most straightforward approach to classifying which projections contribute most to the imaging of a specific configuration is to rely on expert input, such as engineers in industry or doctors in medicine [10]. To reduce the influence of expert subjectivity and enable automation, mathematical model observers can be utilized to detect projections that provide added value to the imaging for the configuration to be examined [11]. The research group of Stayman and Siewerdsen proposes various approaches [9,12] that use the detectability index of the non-prewhitening matched filter (NPWMF) observer as a performance metric for task-based trajectory optimization in C-arm systems for medical imaging. The index is calculated by assessing the trajectory's alignment with a frequency template (task), incorporating both the local modulation transfer function and noise power spectrum. Fischer et al. [13] transfer this approach to industrial CT using projections based on CAD data. Herl et al. introduced a technique in [5] that combines the detectability index with data completeness metrics. Bauer et al. [14] aim to reduce scan time while preserving image quality by utilizing the Fourier transform of reconstructed volumes. Under the assumption that the Fourier coefficients exhibit sparsity, it becomes possible to identify optimal projection directions. Schneider et al. [15] employ a ResNet-34 neural network to predict the detectability index without prior knowledge of the 3D object structure. Based on these predictions, an integer optimization method is applied to generate the trajectory. In [16], Matz et al. propose a geometry-based metric using the discrete wavelet transform of projections for geometry-specific trajectory optimization. A comprehensive overview of the optimization of source-detector trajectories in medical and industrial RCT is documented in [8], therefore this work abstains from duplicating it.

In addition to maximize the information content, it is crucial to ensure that the selected projection views minimize the contribution to the formation of metal artifacts. When X-rays pass through high-density metallic objects, various physical phenomena degrade the image quality and interpretability of the data, chiefly due to photon starvation and beam hardening effects [17]. In addition to the cupping artifact, metal artifacts are characterized by dark and bright streaks in the CT volume [18]. Numerous approaches have been developed to mitigate metal artifacts. While the simplest methods filter out projection views with excessively long X-ray penetration lengths through the object [19], more advanced techniques are also available. For instance, projection-based algorithms reduce the impact of metal artifacts by substituting corrupted projections, induced by metal, with interpolated data derived from neighboring unaffected projections [20–22].

Within the scope of this study, RCT acquisition trajectories are defined based on Herl [23]:

An acquisition trajectory T defines a subset of n projection views $v := \{l_{source}, l_{detector}, o_{source}, o_{detector}\}$, with the source position $l_{source} \in \mathbb{R}^3$, the detector position $l_{detector} \in \mathbb{R}^3$, and the orientations $o_{source} \in \mathbb{R}^3$ and $o_{detector} \in \mathbb{R}^3$, from the set of all possible projection views V . A projection view thus describes the imaging geometry employed for the creation of a specific X-ray projection image.

Existing RCT trajectory optimization methods typically refer to a set of predefined projection views V , which is generated through discretization of a spherical or circular path of constant radius in \mathbb{R}^3 . In

particular, within the realm of highly challenging applications characterized by few-view and limited accessibility RCT scans, existing trajectory optimization algorithms demonstrate shortcomings. Depending on the level of granularity in the discretization of V , optimal views may not be encompassed within V , thus eluding detection by the optimization algorithm. Furthermore, constraints such as trajectory-limiting elements, singularities, or the finite workspace of the industrial robots are often neglected. Several optimization approaches in the literature presuppose the accessibility of all projection views in V , even though in reality, only a subset of V is expected to possess the characteristic of being an accessible projection view. Primarily, it should first be verified whether a projection pose is feasible at all, and only secondarily, which projections achieve high quality. In a previous study [24], we have also demonstrated that utilizing variable distances of the X-ray hardware, as opposed to maintaining constant focus-detector distances, can effectively sample additional object information in challenging-to-access regions.

Therefore, this work introduces an object-specific trajectory optimization approach, which maximizes object geometry depiction for scans in both easily accessible and challenging-to-reach regions. In our methodology, projection views of high information content are identified in the 3D Radon space using a random sample consensus (RANSAC) algorithm [25]. The RANSAC algorithm is a robust parameter estimation method specifically designed to handle datasets with a high proportion of outliers. This approach allows for unconstrained, object-specific projection views, which are no longer limited by discretized initial sets on predefined acquisition geometries. The suppression of metal artifacts is ensured through a local attenuation-based quality control of high-information regions within the projection images. Additionally, projection views are checked for accessibility using an update of the accessibility and collision control introduced in [24].

The algorithm performs particularly well in few-view scan scenarios, where components with distinct edges and flat surfaces are located within highly constrained access areas like in large structural components. This makes the algorithm particularly suitable for target-actual analyses where the prerequisite of prior knowledge of the target state is met such as in the examination of component location, gap analysis or joining points. Furthermore, we would like to point out that, the algorithm is also applicable to optimize few-view scan scenarios of good accessibility.

2. Methodology

According to the herein presented methodology, a high-quality projection view v exhibits the following properties:

- 1) High information content
- 2) Avoiding metal artifacts
- 3) Information novelty
- 4) Accessibility.

The individual properties and their respective assurance are explained in Sections 2.1–2.4 in detail. Fig. 1 illustrates the workflow in a schematic process diagram.

To facilitate comprehension, the scoring principle for the projection views is briefly summarized in the following. After the object under examination is transformed into the 3D Radon space using the 3D Radon transformation, each point in the Radon space corresponds to a plane in the spatial domain. We call these points features. Each feature is assigned an initial weighting of 1. For each reachable projection view selected by the algorithm, the score is defined by the sum of the weights of all features sampled with the specific projection view in the Radon space, as described in Section 2.1. To minimize metal artifacts, the next step involves checking each feature sampled with the specific projection view using simulated X-ray projections to determine if it is located in regions of excessive X-ray absorption. If this is the case, the weight of

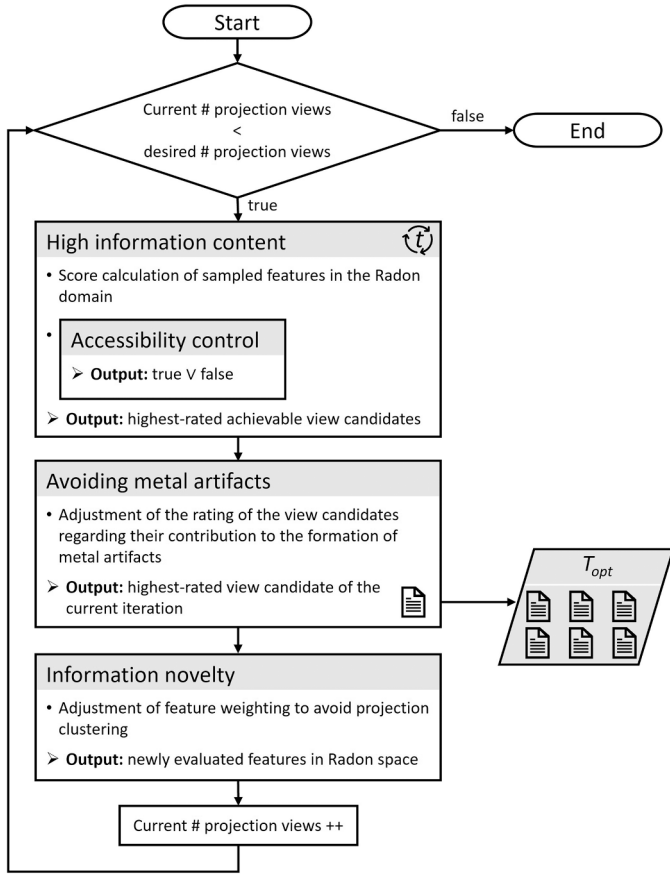


Fig. 1. Schematic representation of the presented workflow for determining object-specific few-view trajectories. The number of iterations within the RANSAC algorithm is represented by t .

these features is set to zero for the current projection view and consequently disregarded for the subsequent score recalculation, see Section 2.2. The projection view with the highest score is added to the trajectory. Before the next iteration, the novelty factor is subtracted from the weighting of the sampled features to avoid projection clustering, as described in Section 2.3.

2.1. High information content

The central hypothesis of our presented methodology is that X-rays tangential to the edges of the object under investigation are essential to adequately reconstruct structures [26,27]. Unlike classical trajectory optimization algorithms, we do not apply a quality criterion to a discrete initial set V as demonstrated e.g. in [4,5,28]. Instead, we derive high-information content projection views directly from CAD data of the object under investigation by utilizing the concept of the 3D Radon transformation. Notable results have already been achieved in cone-beam CT view planning using the 3D Radon transformation.

Amirkhanov and Heinzl employed the 3D Radon transform to identify the optimal object placement in conventional industrial circular CT [19,29]. The approach analyzes the total lost surface area of the object under investigation by assessing how much object information resides outside the torus of measured data in 3D Radon space.

Zheng and Mueller [30] employed the 3D Radon transformation to discern advantageous projection views, targeting dose reduction in the medical domain. Through a set-covering framework, they determined the optimal trajectory, which covers all advantageous views with minimal projection numbers.

Our approach extends existing methods for RCT applications. The

approach aims to identify optimal projection views that can be freely positioned in space and do not involve the constraints of pre-discretized acquisition views and fixed system distances.

Let $f(\vec{x}) \triangleq f(x, y, z)$ denote a 3D object. The 3D Radon transform integrates $f(\vec{x})$ over planes that are defined by the normal vector $\vec{\eta}$ and positioned at a distance c from the origin (center of rotation). The 3D Radon transform is defined by:

$$Rf(\vec{\eta}, c) = \int_{-\infty}^{+\infty} \int_{-\infty}^{+\infty} \int_{-\infty}^{+\infty} f(\vec{x}) \delta(\vec{x}^T \vec{\eta} - c) dx dy dz. \quad (1)$$

Geometrically, the 3D Radon transform establishes a mapping wherein every plane within the spatial domain corresponds uniquely to a point within the 3D Radon space, see Fig. 2. We call these points features. The position vector \vec{p} of the features is determined by the normalized plane normal (direction) and the distance c from the plane to the origin o (length):

$$\vec{p} = c \cdot \frac{\vec{\eta}}{\|\vec{\eta}\|}. \quad (2)$$

Within the Radon space, a cone-beam projection forms the surface of a spherical cap in the imaging ROI. The diameter of the sphere derived from the spherical cap corresponds to the distance from the X-ray source s to the origin (focus-object distance (FOD)). The source position of a corresponding cone-beam projection in the Radon space is determined by:

$$\vec{s} = \frac{\vec{c}_{\text{sphere}}}{\|\vec{c}_{\text{sphere}}\|} \cdot \text{FOD}. \quad (3)$$

The direction of the detector position is determined by the inversion of \vec{s} . The distance of the detector from the origin is defined by the object-detector distance (ODD) which is specified by a ratio value indicating the ratio of FOD and ODD, ensuring that the ROI is fully depicted on the sensitive detector surface with high magnification.

The aim now is to identify those spherical caps (projection views), which intersect o and sample as many high rated features in the Radon space as possible within the permissible error distance d_f from the surface of the spherical cap, see Fig. 4. Each feature is assigned a rating between 0 and 1, which varies depending on how frequently it has been sampled as described in more detail in Section 2.3.

For more intuitive understanding, d_f is approximated for each feature in Radon space using parallel beam geometry in Fig. 3, however the results remain valid for cone-beam CT. For small angles, neighboring radial data lines at distance $|\xi|$ to the origin in the Radon domain are separated by a distance of

$$d_f \approx |\xi| \cdot \Delta\gamma \quad (4)$$

with $\Delta\gamma$ indicating the angular sampling rate [31]. The error tolerance d_f increases with higher distance $|\xi|$. The angular sampling rate can be approximated by

$$\Delta\gamma \approx \frac{\pi}{D} \quad (5)$$

where D describes the number of detector elements imaging the ROI along one detector dimension [31].

The minimum and maximum allowable FOD is represented by d_{\min} and d_{\max} in Fig. 4. It is determined task-specifically by CT specialists.

In the following, the methodology used to identify optimal projection views with high information content is described. We employ a RANSAC algorithm outlined in Table 1 to find optimal spherical caps (projection views) in the Radon space.

The number of iterations t of the RANSAC algorithm is determined empirically. For this, t is varied for the specific test case. The resulting trajectories are simulated, and the corresponding X-ray projection

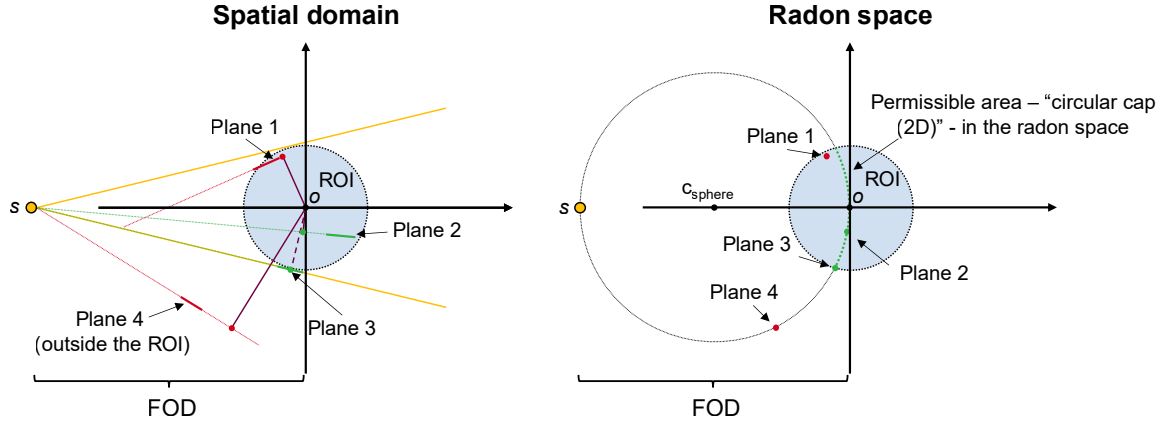


Fig. 2. Sectional Image of a cone-beam CT imaging ROI in the spatial domain (left) and the resulting representation in Radon space (right). Projections in Radon space form so-called circular caps in 2D (spherical caps in 3D). Features representing planes are mapped as a point in the Radon space. Features that intersect the surface of the circular cap are sampled with the corresponding projection view. Adapted from [19].

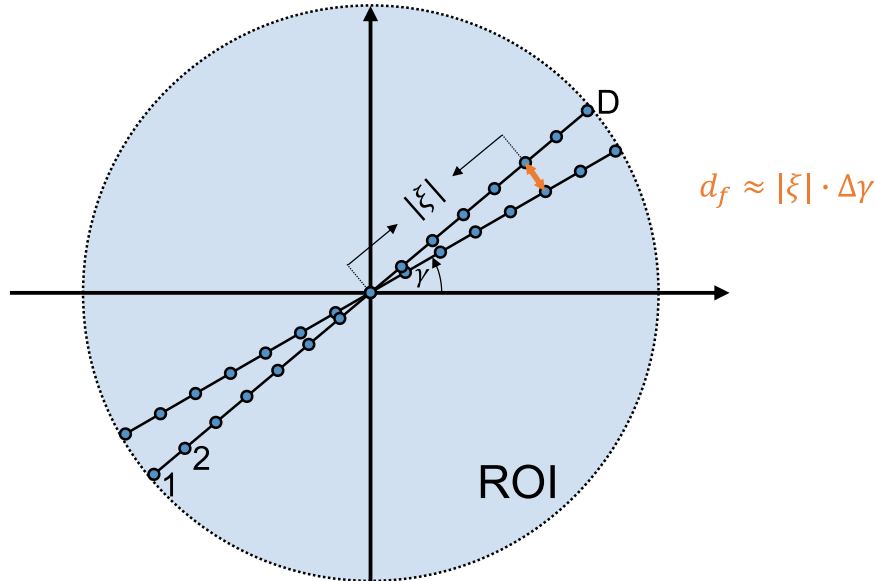


Fig. 3. Radial data lines of parallel beam geometry in Radon space. The approximated allowed error distance of features is described by the product of the distance of features from the origin and the angular sampling rate. Adapted from [31].

images are reconstructed. Theoretically, the best reconstruction corresponds to the optimal t . However, it is observed that for $t > 500$, only marginal improvements occur, accompanied by a substantial increase in computational cost. Therefore, t is set to 500.

2.2. Avoiding metal artifacts

Analogous to the approach of Herl [32], we analyze the X-ray attenuation by locally assessing the contribution of high-information-content pixel regions to the formation of metal artifacts. To generate the attenuation values, we simulate X-ray projection images using the parameters specified for the respective inspection task, utilizing the X-ray simulation software *aRTist* (BAM Federal Institute for Materials Research and Testing) [33]. In this procedure, for the best projection views according to Section 2.1, each feature identified as sampled in Radon space is projected onto the 2D detector utilizing projection matrices:

$$b = P \bullet B \quad (6)$$

with $B = (X, Y, Z, 1)^T$ denoting the feature in Radon space in homoge-

neous world coordinates, P representing the 3×4 projection matrix and $b = (x, y, 1)^T$ denoting the pixel location in homogeneous detector coordinates, which images the feature on the 2D detector. Subsequently, a region with a radius R centered at b is delineated and the residual intensity is assessed to ascertain if it surpasses a predefined minimal intensity threshold. In the context of this work, we adhere to the rule of thumb of maintaining a minimum residual intensity of 10 % of the maximum intensity [34].

If the threshold is not met, the corresponding feature is assigned a weighting of zero (no added value) for this specific projection view. The re-summation of the feature-assigned weightings from the best projection views identified in Section 2.1, after the evaluation in Section 2.2, yields the optimal projection view for the current iteration. Thus, geometrically correctly sampled features in the Radon space, which, however, provide no added value due to excessive absorption, are not included in the calculation of sampled features.

2.3. Information novelty

In order to mitigate the recurrence of sampling identical structures

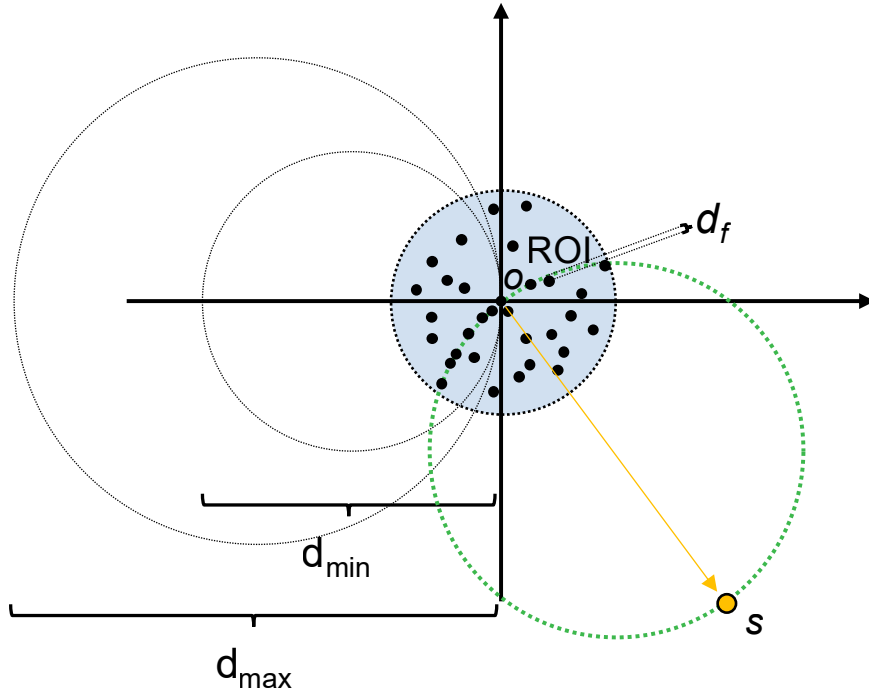


Fig. 4. Sectional Image of a schematic Radon space representation with an ideal source position s .

Table 1

Pseudocode of the utilized RANSAC algorithm for determining optimal projection views.

Algorithm 1 RANSAC for the selection of projection views in 3D Radon space	
1:	Randomly select the data items required to model a sphere. The data items include the origin point, a randomly chosen direction vector for the sphere's center, and a randomly selected radius between $\frac{d_{\min}}{2}$ and $\frac{d_{\max}}{2}$.
2:	Use data items to determine the model parameters (sphere), where the model parameters describe the sphere's center and radius.
3:	Determine the subset of features whose distance to the spherical cap is less than the predefined tolerance d_f . This subset is called the consensus set.
4:	If the scores of the features in the consensus set is higher than the score of the current best sets, include the consensus set within the current optimal sets and remove the least effective of these optimal sets.
5:	Repeat steps 1 through 4 t times

and consequent projection clustering, all features in the Radon space are assigned a weighting $u \in [0, 1]$. In this context, $u_i(z)$ denotes the weighting of feature i at time point z , where i ranges from 1 to G with G denoting the number of features. At the initial stage $u_i(0) = 1$ for all i . For each selected projection view, the following applies:

$$u_i(z+1) = \begin{cases} \max(0, u_i(z) - N), & \text{if feature } i \text{ is sampled} \\ u_i(z), & \text{otherwise} \end{cases} \quad (7)$$

with the novelty factor $N \in [0, 1]$. N represents a static parameter determined empirically. As a general guideline, N should be increased for test objects with a greater number of differently oriented surfaces. This approach ensures effective sampling of as many distinct surfaces as possible.

2.4. Accessibility

Ensuring the accessibility of projection views is crucial for meaningful trajectory planning, particularly in scan regions of limited accessibility. Some RCT trajectory planning algorithms presented assume a discrete set of projection views on a (semi-)sphere as the initial set, e.g. [14]. However, experience shows that typically fewer projection

views are reachable due to potential collisions with the test object, singularities, or the limited workspace of the robots. Similar to the approach of Müller [35], we investigate the accessibility status a_i for each projection view v_i within the iterations of the RANSAC algorithm as follows:

$$a_i = \begin{cases} \text{true}, & \text{if a collision-free inverse kinematics solution exists for } v_i \\ \text{false}, & \text{otherwise.} \end{cases} \quad (8)$$

For the implementation, the RCT-Tool presented in [24] was further developed. CAD-data of the component to be tested is imported into a digital twin of the system. The digital twin represents a replica of the Fraunhofer EZRT system described in [2], including the robot kinematics and X-ray hardware. The linear axes must be manually adjusted when needed. Subsequently, based on the selection of an inspection point, permissible regions (where $a_i = \text{true}$) can be delineated, for both the source and the detector robot separately by presampling possible projection views in space. For that purpose, for each collision-free reachable projection view, where the central ray of the source passes through the center of the ROI and strikes the detector orthogonally at its center, a separate spherical structure is generated for both the detector and the source. For the detector robot, the spherical structure is centered at the detector center, while for the source robot, it is centered at the focal spot. The resulting spherical structures of the detector and those of the source are merged into two separate STL-files using a wrapping tool. Those STL-files represent the collision-free accessible spaces K_s of the source and K_d of the detector respectively. Fig. 5 illustrates the resulting exemplary reachable area of the source (K_s) for the scenario described in Section 3.2.

The tool provides an excellent approximation of collision-free reachable areas. However, for its application on the actual system, it is recommended to manually review critical projection views to account for the error tolerance of several millimeters introduced by the generation of the spherical structures.

By means of raycasting and the odd-even rule of intersections, it is now feasible to verify for every projection view whether the source position is within K_s and the detector position is within K_d . If this is the

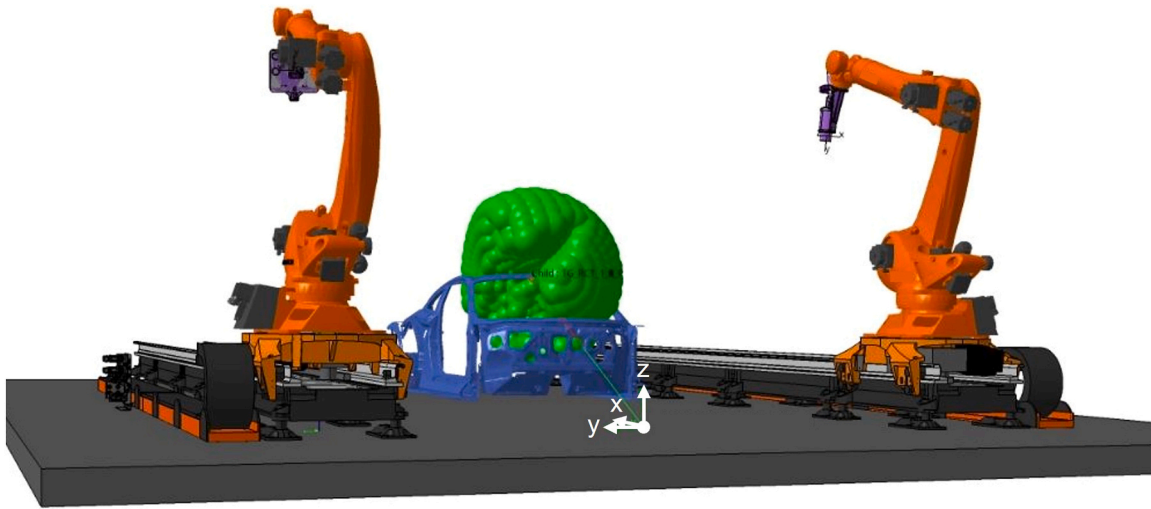


Fig. 5. Illustration of the collision-free accessible space K_s (green) of the source robot for a central imaging point in the area of the windshield frame of a body-in-white as typical example for a large structural component in the automotive sector. Note that there is also a collision-free accessible space K_d for the detector robot, which is not depicted in this graphic.

case, the accessibility status a_i of the corresponding projection view v_i is set to the attribute true. If the boolean attribute a_i carries the value false due to the detector robot, the ODD is iteratively reduced to potentially mark the corresponding projection view v_i as accessible. Increasing the ODD is not feasible due to the imminent risk of incomplete imaging of the ROI on the detector. Modifying the source robot is not viable, as it would alter the analysis of the information quality of the corresponding projection view within the Radon domain.

3. Results

The subsequent section illustrates the advantages of the presented technique over standard trajectories through simulated RCT scans of a reference aluminum component test phantom shown in Fig. 6.

The test phantom encompasses typical features of industrial components. It includes well-defined edges and variously oriented surfaces, a borehole and an elongated slot. In the following, reconstructions of the test phantom using the presented object-specific trajectory optimization approach as well as comparative standard trajectories are analyzed focusing on the quality of edge depiction for classical NDT applications.

We use an equiangular circular trajectory, representing the industry standard, as well as a more advanced spherical trajectory, which distributes the projection views almost uniformly on the sphere's surface based on the concept of the Fibonacci lattice [36] as reference

trajectories. All reference trajectories maintain a constant focus-detector distance (FDD) of 600 mm. The FDD range of the object-specific approach spans from 300 mm to 800 mm. For each object-specific trajectory, 200 projection views are simulated as the expected added value of trajectory optimizations is typically greatest in areas with fewer projections [4,14]. However, it should be noted that the algorithm is also applicable for higher numbers of projections. For the reference trajectories, additional reconstructions with up to 400 projection views are simulated to investigate when these exhibit comparable image quality to the proposed technique.

Two application scenarios are distinguished: Section 3.1 illustrates a scenario of idealized accessibility, while Section 3.2 showcases a RCT scan in a region that is challenging to access.

In addition to qualitative cross-sectional image analysis, we employ the frequently used figure of merit difference of differences in grayscale values of a median-filtered image (DoM) from Kumar et al. [37] on 16 bit cross-sectional reconstructed tiff-images as an indicator for edge sharpness since edge preservation is a crucial factor not only in human visual evaluation [38] but also regarding our use case of geometrical at-line and in-line assembly analysis of large structural components. DoM relies on the variation of grayscale values observed at edges. Higher values indicate a sharper edge representation in the image. We selected this metric due to its superior performance compared to numerous other no-reference sharpness measures, and its strong concordance with

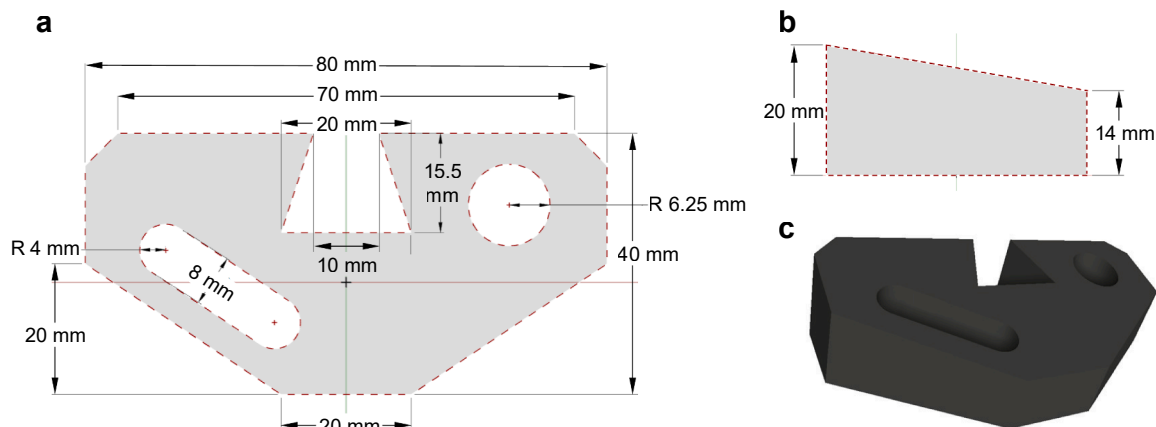


Fig. 6. Technical drawing and 3D visualization of the utilized test specimen. **a:** top-view, **b:** side-view (left), **c:** 3D visualization.

human visual assessment. The *DOM* value is calculated separately for the vertical and horizontal directions. Below, we provide a brief outline of the calculation for the horizontal (x) direction only:

$$DOM_x(x,y) = [I_m(x+2,y) - I_m(x,y)] - [I_m(x,y) - I_m(x-2,y)]. \quad (9)$$

Here, $I_m(x,y)$ denotes the grayscale value of a pixel at coordinates (x,y) within a median-filtered image.

The *DOM*-based sharpness in the x-direction, $S_x(x,y)$, for a pixel at position (x,y) in an image is then calculated as:

$$S_x(x,y) = \frac{\sum_{x-w \leq q \leq x+w} |DOM_x(q,y)|}{\sum_{x-w \leq q \leq x+w} |I(q,y) - I(q-1,y)|} \quad (10)$$

where $w = 2$ represents the window size describing the edge width and $I(q,y)$ denotes the value of the pixel located at (q,y) in the image. Based on a threshold value of 0.0001, it is determined whether the respective pixel is sharp. Once $S_x(x,y)$ and $S_y(x,y)$ have been calculated, the overall sharpness of the image S_I is determined by:

$$S_I = \sqrt{\left(\frac{\#sharp\ pixels_x}{\#edge\ pixels_x}\right)^2 + \left(\frac{\#sharp\ pixels_y}{\#edge\ pixels_y}\right)^2}. \quad (11)$$

For a more detailed description, we refer the curious reader to [37].

Additionally, we apply the accumulated deviation distribution from nominal-to-actual comparisons in *VGSTUDIO MAX 2023.4 (Volume Graphics GmbH)* of the reconstructed volumes with the CAD model of the component as an application oriented quantitative metric for the imaging accuracy of object surfaces. In this process, the percentage of surface conformity is analyzed up to an allowable deviation of 100 μm . We establish 100 μm as the threshold as it is a commonly encountered resolution requirement in the industry. For the required surface determination in the scenario of idealized accessibility, the Iso-50 value method is employed, where only air and the component's material, namely aluminum, are present. For the scenario of challenging accessibility, we use the advanced surface determination module with the ground truth CAD as the initial contour and a searching distance of 20 voxels, corresponding to 2 mm. The search distance was intentionally set relatively high to minimize the proportion of false positive gradient determinations that could occur with smaller search radii. Quantitative results are presented in projection-quality curves that compare the trajectories for each of the employed metrics.

For the simulations, the following X-ray parameters are set: The acceleration voltage is set to 225 kV, the tube current is set to 0.22 mA to fully utilize the power limit of the smallest focal spot of the simulated source. The exposure time is automatically adjusted by the X-ray simulation software *arTist* so that a background intensity of 90 % of the maximum gray value is maintained for each gain image. A flat-field correction is automatically performed for each projection. A 3000×3000 pixel² flat panel detector with a pixel size of 0.1 mm is

used. A 0.5 mm Cu filter is applied. The ROIs are reconstructed into CT volumes using a voxel grid of $1000 \times 1000 \times 1000$ with a voxel size of 0.1 mm. All reconstructions are performed with the algebraic reconstruction technique (ART) inherent in the *CERA 6* CT imaging software (*Siemens Healthineers AG*). The novelty factor N is set to 0.2.

3.1. Scenario of idealized accessibility

In this scenario, apart from the test phantom, no further trajectory-limiting elements are present. It represents an idealized scenario of full accessibility. Fig. 7 shows the source positions of the three comparison trajectories for an exemplary size of 20 projection views. It becomes evident that projection clustering is avoided effectively using the novelty factor in the presented methodology, and that various features must be sampled with the projection views as a wide variety of projection directions are integrated.

Fig. 8 presents exemplary sectional images of reconstructions from 20, 60 and 200 projection views for qualitative visual analysis of each trajectory. As expected, the edge representation appears sharper across all trajectories with an increasing number of views. This is because more object information is sampled, raising the likelihood of tangentially sampling edges of the object under investigation with X-rays with the standard trajectories. For the object-specific approach, specific edges are tangentially sampled with each view. The more views integrated into the object-specific trajectory, the more edge information can be captured. When comparing the trajectory sampling methods, the presented approach produces the sharpest impression for prominent edges and appears the least blurred. The regions appearing the most blurred are the edges of the borehole and the slot. This is typical for geometry- and object-specific trajectory optimization approaches, as the many divergent orientations in curved edges require many projection views for optimal sampling, which cannot be achieved with the limited number of projection views in this case.

The quantitative image quality analysis (IQA), focusing on the edge sharpness in reconstructed cross-sectional images of the central plane using the *DoM* value, confirms the visual impressions of Fig. 8. Fig. 9 illustrates the results in projection-quality curves of the top-view and the side-view respectively. For comparison, the *DoM* value of a fully accessible circular trajectory with 2880 projections was also included as the ground truth trajectory. The findings demonstrate that the optimized trajectory significantly outperforms both reference trajectories in terms of resulting edge sharpness, especially in the few-view cases. It is noteworthy that the reference trajectories exhibit relatively small deviations from each other up to 200 projections (on average, a delta of 0.0094 in *DoM* IQA value), while the presented trajectory optimization technique is rated, on average, 0.049 *DoM* IQA value points higher than the mean of the reference trajectories.

Particularly for the presented object-specific views approach, the projection-quality curves exhibit an asymptotic behavior towards the

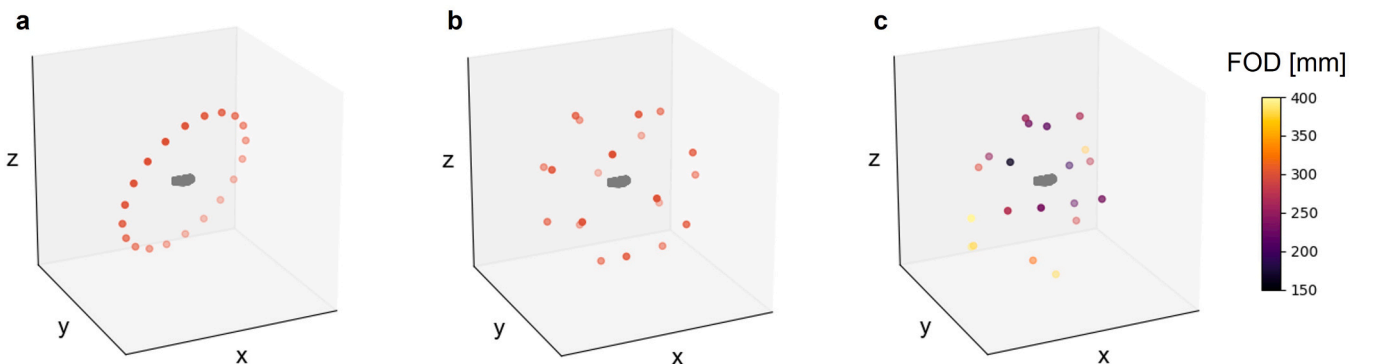


Fig. 7. Resulting source positions of the comparison trajectories at 20 projection views. a: Circular trajectory, b: Fibonacci sampled spherical trajectory, c: Object-specific views approach.

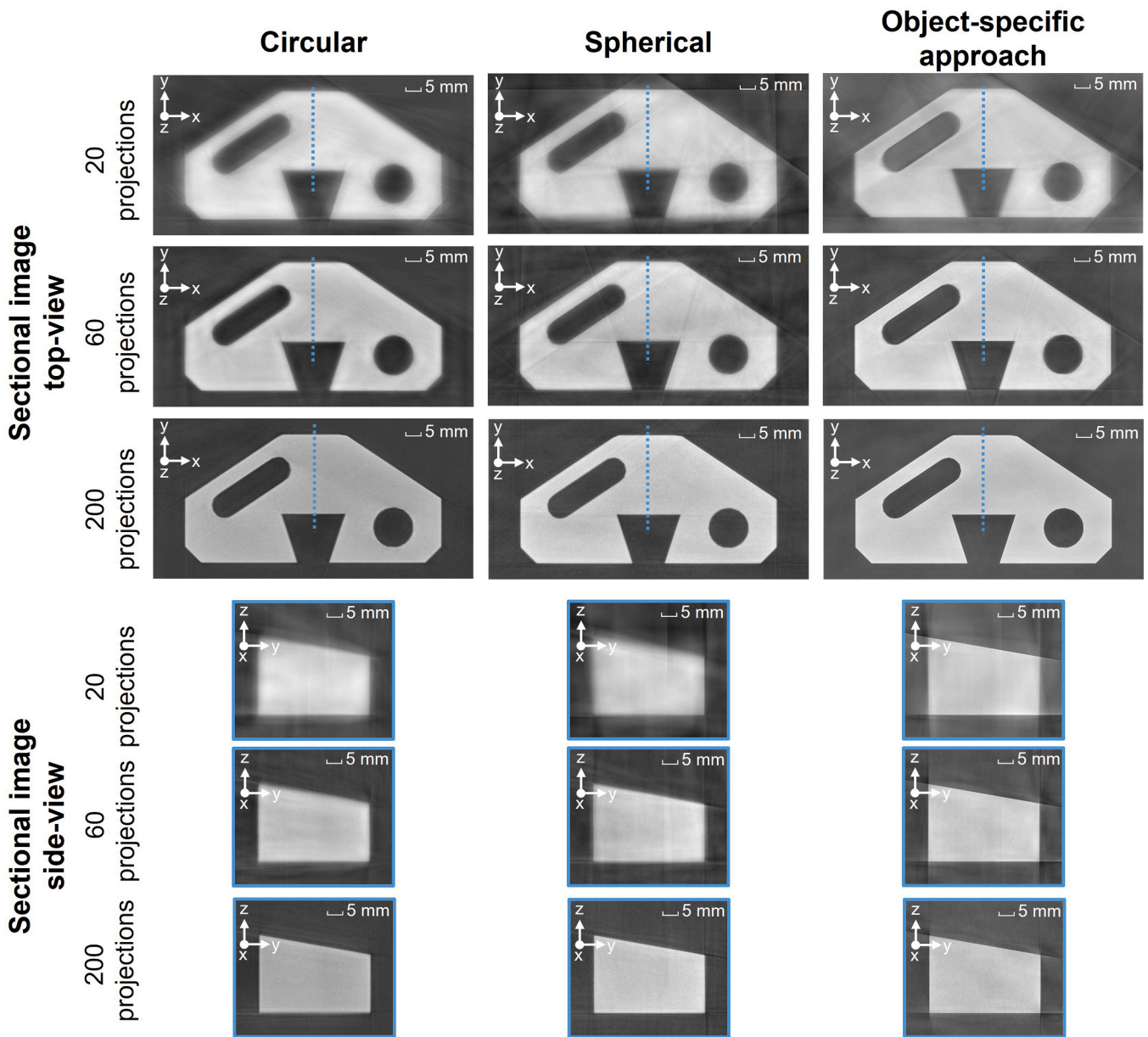


Fig. 8. Exemplary sectional images of the CT reconstructions of the different trajectories. Each sectional image depicts views through the central plane.

ground truth. As typical for trajectory optimizations, most significant improvements in quality occur with a small number of projections. This is because the primary features of the object under investigation can often be accurately captured with a small number of projections, whereas finer spherical or circular features require a larger number of projections for accurate representation. Consequently, the persistent gap between the ground truth and the comparative trajectories can be justified.

Furthermore, the IQA curve of the side view of the spherical trajectory shows a fluctuating behavior, especially in the low projection range. Such a fluctuation can occur especially in the spherical trajectory, since an approximately equidistant distribution of projection views on the sphere is achieved for each trajectory size. It is therefore possible that a trajectory of size n captures more edge information of the object under investigation than a trajectory of size $n + x$, as the projection directions fundamentally change. This behavior is only weakly observable in the circular trajectory, as the trajectory's orientation remains constant, and only the sampling within the circular plane influences edge detection on an intra-category level.

The results of the application-oriented metric in Fig. 10, which evaluates the congruence of the reconstructed volume's surface with the ground truth CAD model, further corroborates the observations. It also confirms the significantly superior performance of the presented trajectory optimization method compared to the other trajectories for every trajectory size evaluated. The asymptotic behavior of the projection-quality curves is observed for the same reasons as noted in the analysis of the DoM IQA value. With the integration of just 60 projections, the presented method achieves 100 % surface conformity within the specified error tolerance of $100 \mu\text{m}$. The reference trajectories fall significantly short of this value, exhibiting an average of 14.61 % and up to 35.72 % worse surface alignment in the reconstructed volumes up to trajectory sizes of 200 projection views, compared to those achieved with the presented object-specific trajectory optimization. As with the analysis of the IQA value, it is noticeable that the added value of the method presented is higher with small projection numbers. To fully depict the reconstructed volume within the allowed error tolerance, the spherical trajectory requires at least 90 additional projections for the depicted test case, while the circular trajectory still fails to achieve

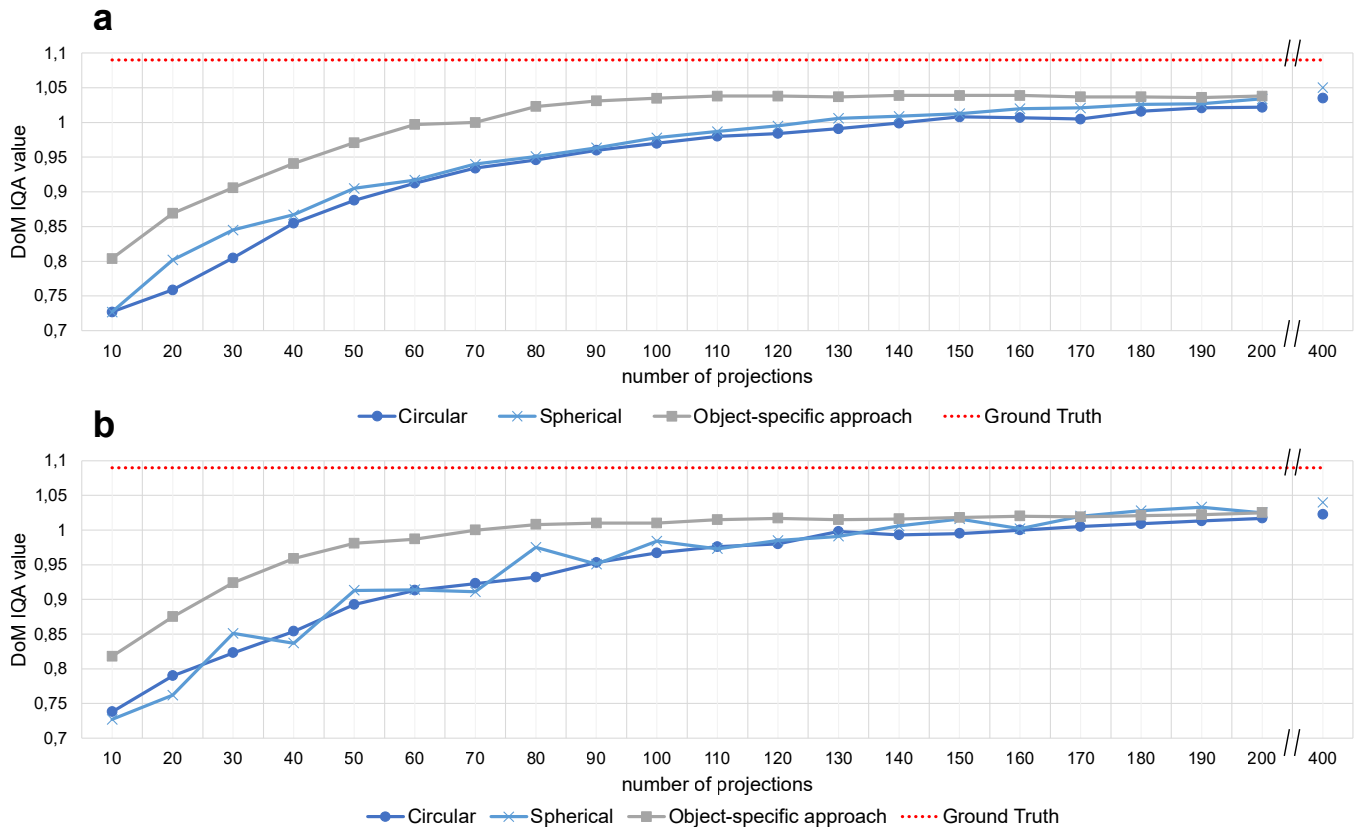


Fig. 9. Results of the quantitative image quality analysis between the trajectories based on the DoM sharpness estimation metric from [37](a: top-view, b: side-view).

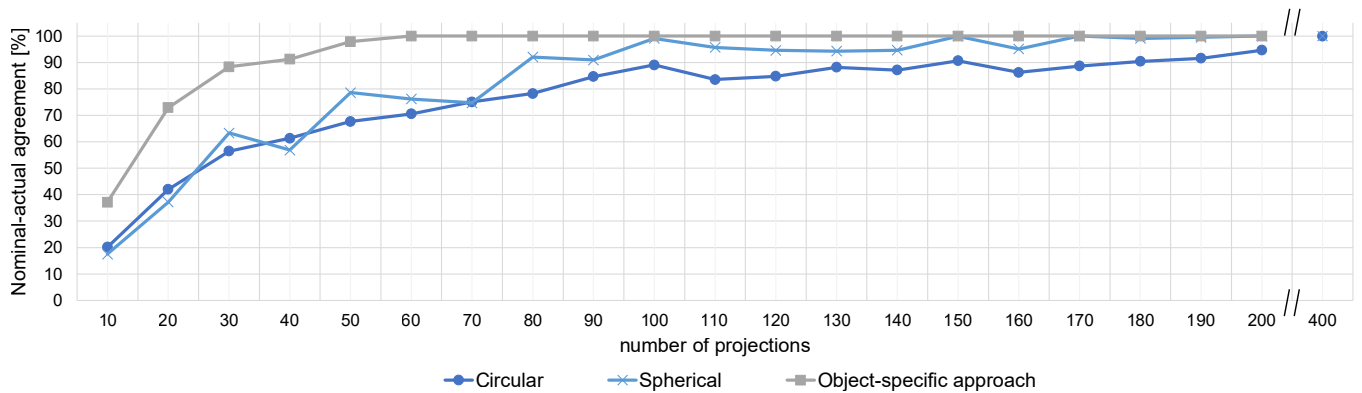


Fig. 10. Nominal-actual comparison of the reconstructed volumes resulting from the trajectories with a deviation of less than 100 μm from the ground truth CAD model.

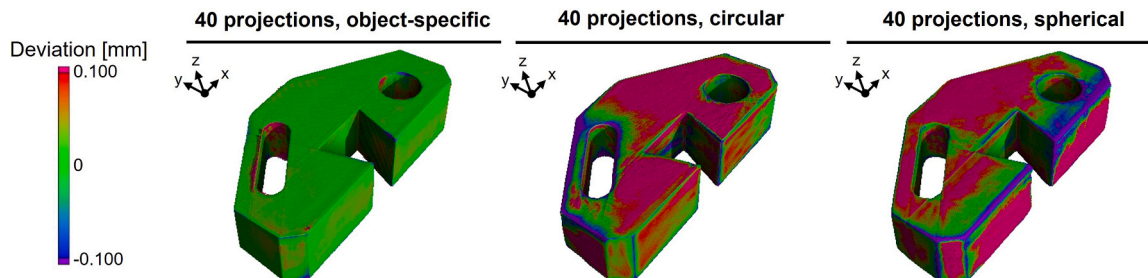


Fig. 11. False-color representation of the nominal-actual comparison calculated from the reconstructed volumes for the trajectories being compared, based on a trajectory size of 40 projection views.

complete agreement even after 200 projections.

Fig. 11 highlights the added value of our technique in the nominal-to-actual comparison for few-view scenarios using a false-color representation for an exemplary trajectory size of 40 projection views. It is noteworthy that the proposed technique was already able to adequately represent the planar primary surfaces with just 40 views, resulting in an overall surface agreement of 91.24 %. However, curved geometric regions, such as the borehole, still exhibit incomplete agreement.

3.2. Scenario of challenging accessibility

In this scenario, the test phantom is positioned in a challenging-to-access region within the windshield frame of a body-in-white. The placement of the test object beneath the windshield frame, composed of steel and aluminum, can be observed in the X-ray projection image of the test body shown in Fig. 12.

This setup exemplifies a scenario characterized by restricted accessibility, commonly encountered in RCT scans of large components. Fig. 5 illustrates the test scenario, including the regions that can be reached by the source robot without collisions. Fig. 13 illustrates the comparison trajectories for 20 projection views. The tilting of the circular trajectory was designed to ensure that as many projection views as possible lie within the accessible area. It is ensured that the comparison trajectories consist of the same number of projection views as the object-specific approach. As depicted in Fig. 13, the necessary projection views are distributed across the accessible regions.

It becomes especially evident in the circular trajectory design, that views are missing in the windshield frame as well as in the immersion area of the windshield due to potential collisions and accessibility constraints. In general, all trajectory designs lose projection direction possibilities due to this reason.

For the perceptual performance analysis, exemplary resulting sectional images of the test specimen are presented in Fig. 14. Compared to the cross-sectional images of the region of idealized accessibility in Fig. 8, some additional artifacts are observed in the datasets due to the surrounding geometries of the body-in-white, which are primarily composed of steel and aluminum.

However, it is also observable in this scenario that the images appear

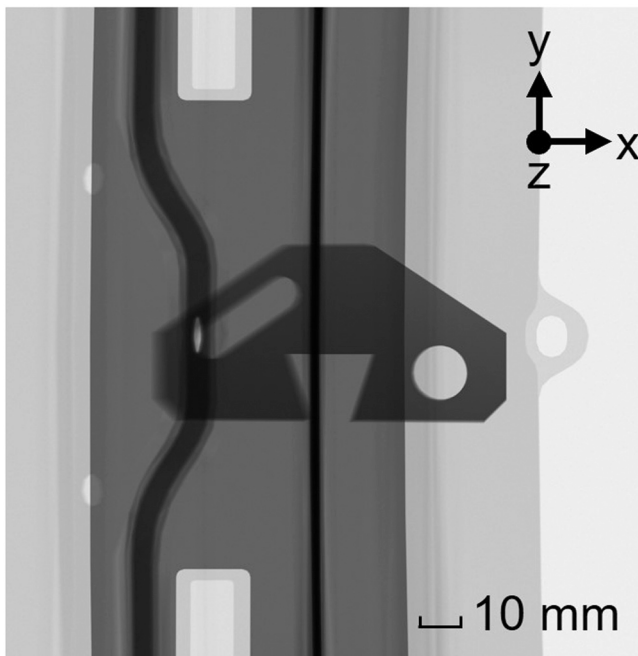


Fig. 12. exemplary X-ray projection image showing the test specimen placement beneath the windshield frame.

sharper across all trajectories with an increasing number of projections. The reconstructions from the circular and spherical trajectory designs convey a similar quality impression to the human observer. This observation can be explained by the fact that both trajectory designs, with such a limited number of projections, are capable of depicting the coarse geometry of the object. The precise tangential sampling of object planes can, however, occur only by an exceedingly rare coincidence. The edge depiction of the reconstructions of the object-specific trajectory design presented in this work also appear sharpest in this scenario. In the 20-view representation of the object-specific approach, it is observed that the largest planar surfaces in the object (the upper and lower edges in the side view) already appear very sharp, while other edges corresponding to smaller areas (see top view) are not yet sharply delineated. This is attributable to the algorithm's search for projection views with the highest ranking in the Radon space (see Section 2). Consequently, projections that sample larger surfaces are incorporated into the trajectory at an earlier stage. In the top-view sectional image of the 60-view reconstruction of the object-specific approach, it becomes apparent that an increasing number of projections enhances the sharpness of smaller areas. Furthermore, it is once again evident that the variety of tangents associated with the elongated slot and the borehole presents the greatest challenges. Due to this tangent diversity, multiple projection views are required to fully capture these areas. As the number of projections increases, these regions are also represented sharper.

Fig. 15 confirms the visual impressions by presenting the corresponding results of the investigation of edge sharpness as projection-quality curves for both the top and side views. For reference, the *DoM* value obtained from a fully accessible circular trajectory comprising 2880 projections is again included, serving as the ground truth trajectory.

The results clearly indicate that the optimized trajectory yields superior edge sharpness compared to both reference trajectories especially in areas of low projection numbers. The quality of edge representation improves with an increasing number of projections across all trajectory forms. The higher the number of projections, the more the curves of the trajectories converge. The deviation of the reference trajectories, averaging 0.00429 in the *DoM* IQA value for up to 200 projection views, is significantly smaller than the average performance improvement of 0.0419 *DoM* value points exhibited by the optimized trajectory over the same range when compared to the mean of the reference trajectories. The comparative analysis of the *DoM* values between this scenario and the idealized accessibility scenario discussed in Section 3.1 reveals that the absolute differences between the trajectory optimization and the reference trajectories are remarkably similar. Additionally, it becomes evident that the performance of all trajectory designs is diminished in the scenario of limited accessibility. This performance decline is attributable to the reduction in available projection directions resulting from the incorporation of reachability and collision constraints as well as the additional X-ray interactions with supplementary object geometry of the body-in-white.

Moreover, the results of the matching object surface analysis with a maximum deviation of 100 μm , shown in Fig. 16, provide additional confirmation of the enhanced performance achieved by the trajectory optimization technique introduced in this study. Throughout the entire range of up to 200 projection views, the reference trajectories are significantly outperformed. Similar to the edge sharpness metric, the superior performance is particularly pronounced at low projection numbers. With a trajectory size of 50 views e.g., 85.7 % of the object surface is already accurately depicted according to the metric, while the reference trajectories can only achieve matches of 52.1 % and 51.3 %, respectively. The top rating of the object-specific trajectory is less than the 100 % accuracy observed in the idealized scenario described in Section 3.1. This is attributable to the challenging scan conditions imposed by additional collision elements and the presence of highly absorbing materials. In such scenarios, achieving 100 percent agreement is challenging, as evidenced by the values of the comparison trajectories

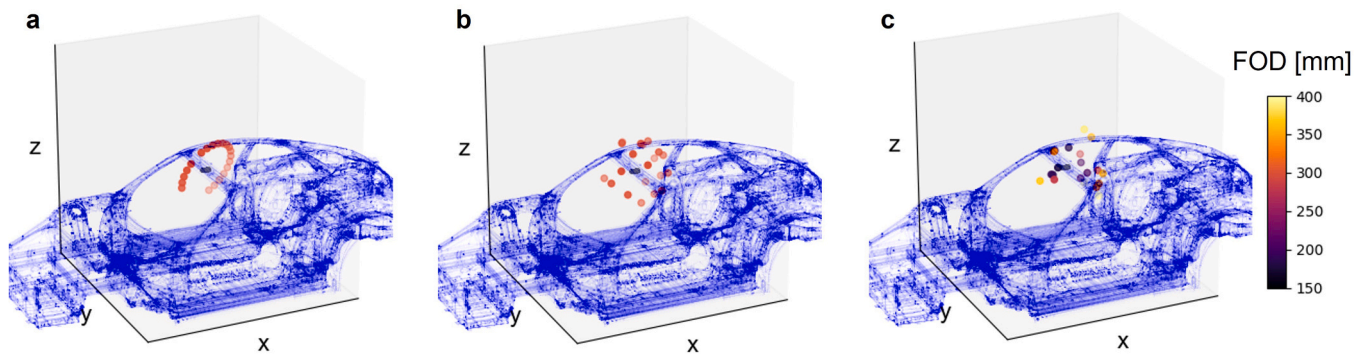


Fig. 13. Resulting source positions of the comparison trajectories at 20 projection views in the limited accessibility scenario. a: Circular trajectory, b: Fibonacci sampled spherical trajectory, c: Object-specific views approach.

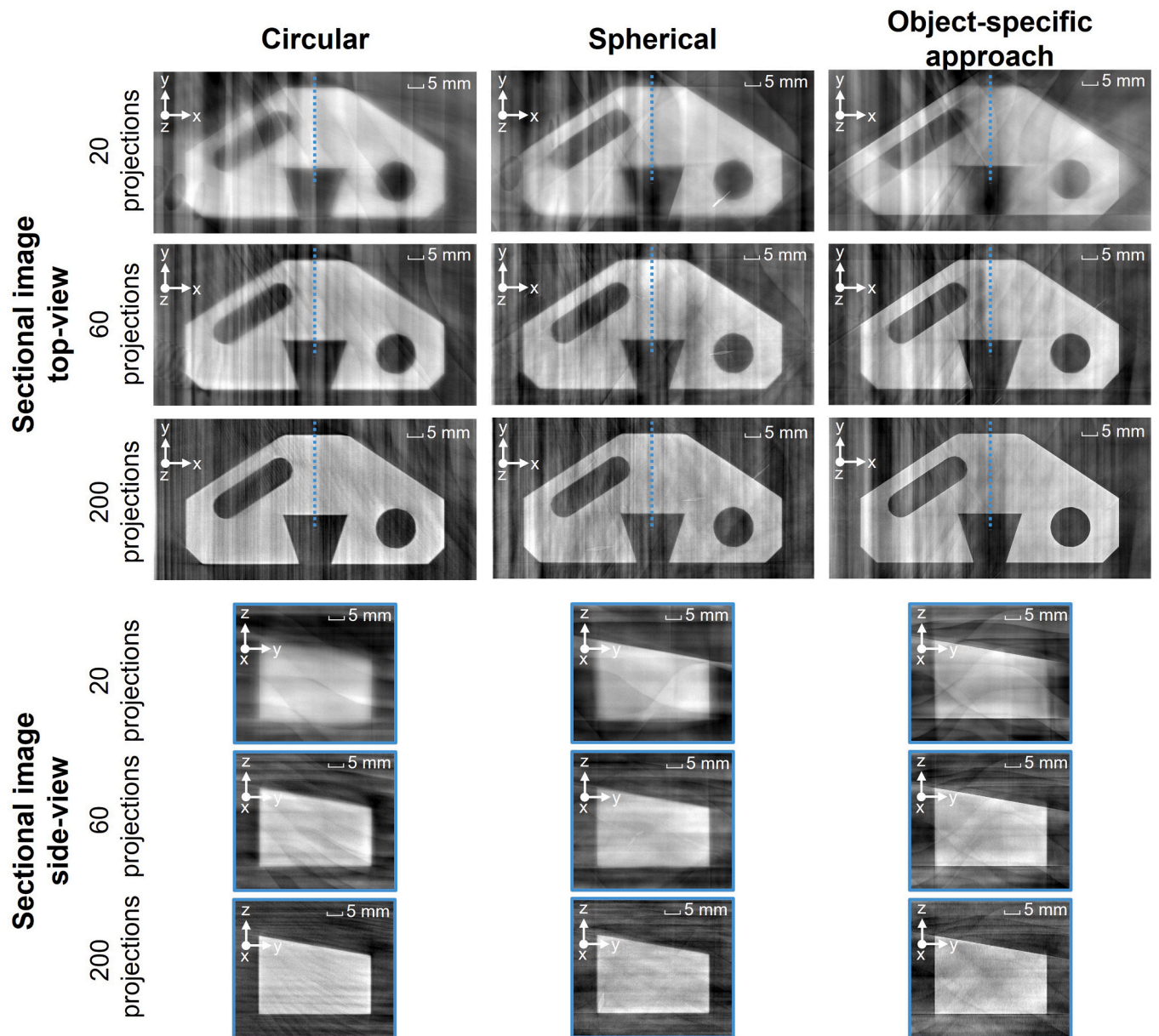


Fig. 14. Exemplary sectional images of the CT reconstructions of the different trajectories. Each sectional image depicts views through the central plane.

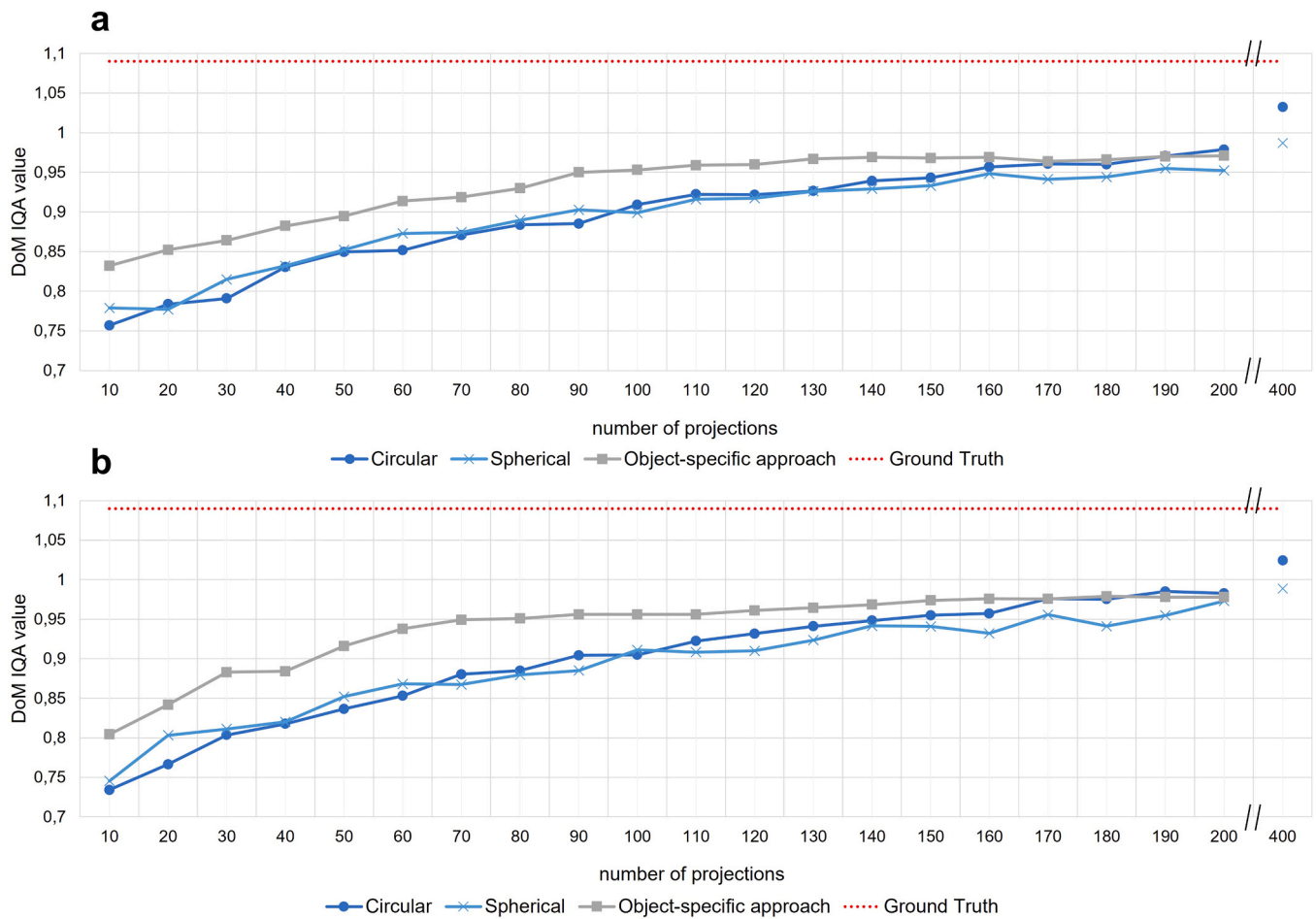


Fig. 15. Results of the quantitative image quality analysis between the trajectories in the scenario of challenging accessibility based on the DoM sharpness estimation metric from [37] (a: top-view, b: side-view).

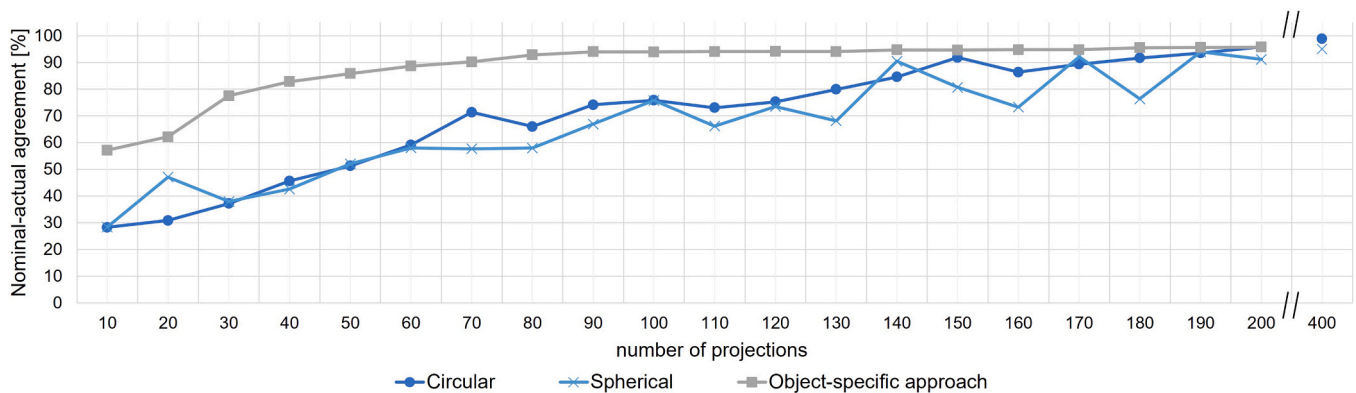


Fig. 16. Nominal-actual comparison of the reconstructed volumes in the scenario of challenging accessibility resulting from the trajectories with a deviation of less than 100 μm from the ground truth CAD model.

even at 400 projections. Furthermore, it should be noted that the intersectional results of this application-oriented metric are not directly comparable, as a different surface determination method had to be employed due to the multi-material scenario in this section. On average, the optimized trajectory exhibits a 20.37% higher matching to the ground truth compared to the reference trajectories up to 200 projections, with a maximum up to 40.3% better surface alignment. Once again, the unique strength of the proposed technique becomes evident, particularly in few-view scenarios.

Fig. 17 once more highlights the added value of our technique in the nominal-to-actual comparison for few-view scenarios using a false-color representation for an exemplary trajectory size of 40 projection views. The proposed technique demonstrates its capability to accurately capture the planar primary surfaces using only 40 views, achieving an overall surface agreement of 82.81% while both the circular and spherical trajectories exhibit approximately 40% worse surface agreement.

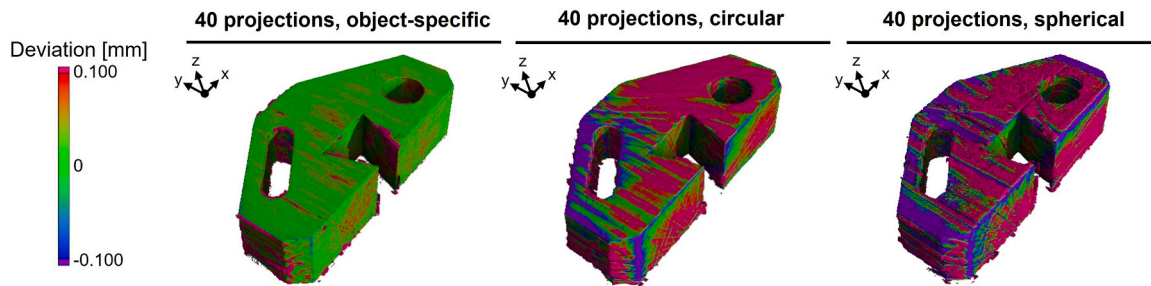


Fig. 17. False-color representation of the nominal-actual comparison for the scenario of challenging accessibility calculated from the reconstructed volumes for the trajectories being compared, based on a trajectory size of 40 projection views.

4. Conclusion

In this paper, we introduced a trajectory optimization technique based on a 3D Radon space analysis, designed to identify optimized object-specific trajectories capable of sharp edge reconstruction and artifact suppression for robot-based CT in few-view scenarios. Unlike existing approaches, our solution does not apply an objective function to discrete projection views on predefined acquisition geometries but instead enables the determination of optimal projection views freely within the space. Due to the elimination of discretization, our technique has the significant advantage that certain planes of objects can potentially be optimally tangentially sampled, which might not be possible with quality criteria based on discrete imaging geometries. In the latter case, the optimal projection view may lie exactly between two discrete projection views, and thus can never be detected. Thus, we eliminate the impact of discretizing the initial set and benefit from integrating acquisition directions under flexible distance configurations that would lead to collisions in trajectories of fixed distance configurations. This advantage is especially beneficial for scans of subregions within large structural components. Our technique requires CAD and material data of the object under investigation, as well as the region to be imaged, as input. It then outputs optimized projection views, including optimized collision-free positions and corresponding orientations of the source and the detector for any trajectory size specified by the user or required by a given cycle time.

For our optimization approach, we defined four key criteria to determine the ideal projection views. First, we ensure a high level of information content by analyzing the number of sampled features in the 3D Radon space for each projection view. Additionally, we filter out projection views that are likely to contribute to the formation of metal artifacts by performing a local, X-ray image-based residual intensity analysis of grayscale values in high-information-content areas. To ensure information novelty, we devalue previously sampled features in the Radon space using a novelty factor. Finally, we ensure the collision-free accessibility of the projection views within the digital twin.

We compare the presented technique against two benchmark trajectories (equiangular circular trajectory and fibonacci sampled spherical trajectory) with respect to the resulting image quality for trajectory sizes up to 200 projection views in both a scenario of idealized accessibility and a scenario of limited accessibility. We limited the comparison to 200 projection views, as previous studies have demonstrated that the benefits of object-specific trajectory optimization are most effectively illustrated within this range of trajectory sizes [4,28]. Moreover, in automotive production, the cycle times required for at-line or in-line CT inspections can typically only be met with few-view CT approaches. The reference trajectories were significantly outperformed by our technique in both the edge sharpness metric [37] and the application-oriented metric of percentage surface agreement of the reconstructions with the CAD ground truth in both scenarios. Additionally, the qualitative comparison of the resulting reconstructions strongly supports the quantitative analyses, highlighting the superior sharpness

achieved with the proposed technique. As a test specimen, we designed a test phantom, which incorporates typical features of industrial objects, such as salient edges, as well as a borehole and an elongated slot.

While our presented approach enhances the imaging sharpness of salient, straight edges, it faces the typical challenge of geometry-specific trajectory optimizations of accurately imaging curved edges, as observed in the regions of the borehole and the elongated slot. This issue arises because curves are converged by numerous tangents, requiring corresponding X-rays for accurate reconstruction. However, a variety of industrial applications still present significant potential for object-specific trajectory optimization, particularly when distinct regions of an object must be reconstructed with high quality, such as in the examination of component location, gap analysis or joining points. In particular, the inspection of multiple large components with identical geometries in industrial quality assurance using robot-based CT is ideally suited for our approach.

For general defect analysis or damage forensics applications, methodologies that utilize significantly more projection views to achieve comprehensive sampling of the imaging region are more appropriate, as the damage pattern is unknown and therefore cannot be represented in the 3D Radon space.

Funding

This work was funded by the Dr. Ing. h.c. F. Porsche AG and facilitated through collaborative research between academia and industry in partnership with the University of Augsburg.

CRediT authorship contribution statement

Linde Maximilian: Writing – original draft, Visualization, Validation, Software, Methodology, Data curation, Conceptualization. **Wiest Wolfram:** Writing – review & editing, Supervision. **Trauth Anna:** Writing – review & editing, Supervision. **Sause Markus G. R.:** Writing – review & editing, Supervision.

Declaration of Competing Interest

The authors declare the following financial interests/personal relationships which may be considered as potential competing interests: Maximilian Linde has patent pending to Dr. Ing. h.c. F. Porsche AG. If there are other authors, they declare that they have no known competing financial interests or personal relationships that could have appeared to influence the work reported in this paper.

Acknowledgments

We would like to thank the EngRoTec Consulting GmbH for the implementation of the advancements of the RCT tool.

Data availability

The research data cannot be disclosed as it constitutes the proprietary information of the Dr. Ing. h.c. F. Porsche AG.

References

- [1] U. Ewert, T. Fuchs, *Progress in digital industrial radiology, Pt. 2, Comput. Tomogr. (CT)*, Badania Nieniszczące i Diagn. (2017) 7–14.
- [2] W. Holub, F. Brunner, T. Schön, Roboct-application for in-situ inspection of joint technologies of large scale objects, in: *International Symposium on Digital Industrial Radiology and Computed Tomography*, 2019, pp. 1–7.
- [3] A. Ziertmann, P. Jahnke, W. Holub, RoboCT-production monitoring in automobile industry 4.0, in: *Sonderband "ZfP heute" als Ersatz für die abgesagte DGZfP Jahrestagung 2020*, 2020, pp. 22–26.
- [4] F. Bauer, D. Forndran, T. Schromm, C.U. Grosse, Practical part-specific trajectory optimization for robot-guided inspection via computed tomography, *J. Nondestruct. Eval.* 41 (2022) 55, <https://doi.org/10.1007/s10921-022-00888-9>.
- [5] G. Herl, J. Hiller, M. Thies, J.-N. Zaech, M. Unberath, A. Maier, Task-specific trajectory optimisation for twin-robotic X-ray tomography, *IEEE Trans. Comput. Imaging* 7 (2021) 894–907, <https://doi.org/10.1109/TCL.2021.3102824>.
- [6] I.G. Kazantsev, *Information content of projections in few-views tomography*, *Proc. SPIE* (1992) 62–64.
- [7] F. Bauer, *Trajectory Optimization for Sparsely Sampled Computed Tomography*, 2022.
- [8] S. Hatamikia, A. Biguri, G. Herl, G. Kronreif, T. Reynolds, J. Kettenbach, T. Russ, A. Tersol, A. Maier, M. Figl, J.H. Siewerdsen, W. Birkfellner, Source-detector trajectory optimization in cone-beam computed tomography: a comprehensive review on today's state-of-the-art, *Phys. Med. Biol.* 67 (2022) 16TR03, <https://doi.org/10.1088/1361-6560/ac8590>.
- [9] J.W. Stayman, S. Capostagno, G.J. Gang, J.H. Siewerdsen, *Task-driven source-detector trajectories in cone-beam computed tomography: I. Theory and methods*, *J. Med. Imaging* 6 (2019) 25002.
- [10] F.R. Verdun, D. Racine, J.G. Ott, M.J. Tapiovaara, P. Toroi, F.O. Bochud, W.J. H. Veldkamp, A. Schegerer, R.W. Bouwman, I.H. Giron, others, Image quality in CT: from physical measurements to model observers, *Phys. Med.* 31 (2015) 823–843.
- [11] H.H. Barrett, J. Yao, J.P. Rolland, K.J. Myers, Model observers for assessment of image quality, *Proc. Natl. Acad. Sci.* 90 (1993) 9758–9765.
- [12] Jeffrey H. Siewerdsen, *Task-Based Trajectories in Iteratively Reconstructed Interventional Cone-Beam CT*, in:
- [13] A. Fischer, T. Lasser, M. Schrapp, J. Stephan, P.B. Noël, *Object specific trajectory optimization for industrial x-ray computed tomography*, *Sci. Rep.* 6 (2016) 19135.
- [14] F. Bauer, M. Goldammer, C.U. Grosse, Scan time reduction by fewer projections-an approach for part-specific acquisition trajectories, in: *20th World Conference on Non-Destructive Testing*, 2020.
- [15] L.-S. Schneider, M. Thies, R. Schielein, C. Syben, M. Unberath, A. Maier, *Learning-based Trajectory Optimization for a Twin Robotic CT System*, *Proc. 12th Conf. Ind. Comput. Tomogr. (iCT)* (2022) 1–8.
- [16] A. Matz, W. Holub, R. Schielein, *Trajectory optimization in computed tomography based on object geometry*, in: *11th Conference on Industrial Computed Tomography, Wels, Austria (iCT 2022)*, 2022.
- [17] M. Katsura, J. Sato, M. Akahane, A. Kunimatsu, O. Abe, *Current and novel techniques for metal artifact reduction at CT: practical guide for radiologists*, *Radiographics* 38 (2018) 450–461.
- [18] J.F. Barrett, N. Keat, *Artifacts in CT: recognition and avoidance*, *Radiographics* 24 (2004) 1679–1691.
- [19] A. Amirkhanov, C. Heinzl, M. Reiter, E. Gröller, *Visual optimality and stability analysis of 3DCT scan positions*, *IEEE Trans. Vis. Comput. Graph.* 16 (2010) 1477–1486.
- [20] M. Bazalova, L. Beaulieu, S. Palefsky, F. Verhaegen, *Correction of CT artifacts and its influence on Monte Carlo dose calculations*, *Med. Phys.* 34 (2007) 2119–2132.
- [21] Y. Chen, Y. Li, H. Guo, Y. Hu, L. Luo, X. Yin, J. Gu, C. Toumoulin, others, *CT metal artifact reduction method based on improved image segmentation and sinogram in-painting*, *Math. Probl. Eng.* 2012 (2012).
- [22] E. Meyer, R. Raupach, M. Lell, B. Schmidt, M. Kachelrieß, *Normalized metal artifact reduction (NMAR) in computed tomography*, *Med. Phys.* 37 (2010) 5482–5493.
- [23] G. Herl, *Multipositional x-ray tomography for avoidance and reduction of image artefacts*, 2022.
- [24] M. Linde, W. Wiest, A. Trauth, M.G.R. Sause, *Selecting feasible trajectories for robot-based X-ray tomography by varying focus-detector-distance in space restricted environments*, *J. Nondestruct. Eval.* 43 (2024) 65, <https://doi.org/10.1007/s10921-024-01075-8>.
- [25] M.A. Fischler, R.C. Bolles, *Random sample consensus: a paradigm for model fitting with applications to image analysis and automated cartography*, *Commun. ACM* 24 (1981) 381–395.
- [26] H.K. Tuy, *An inversion formula for cone-beam reconstruction*, *SIAM J. Appl. Math.* 43 (1983) 546–552.
- [27] E.T. Quinto, *Singularities of the X-ray transform and limited data tomography in R² and R³*, *SIAM J. Math. Anal.* 24 (1993) 1215–1225.
- [28] F. Bauer, M. Goldammer, C.U. Grosse, *Selection and evaluation of spherical acquisition trajectories for industrial computed tomography*, *Proc. R. Soc. A* 477 (2021) 20210192.
- [29] C. Heinzl, J. Kastner, A. Amirkhanov, E. Gröller, C. Gusenbauer, *Optimal specimen placement in cone beam X-ray computed tomography*, *NDT E Int.* 50 (2012) 42–49.
- [30] Z. Zheng, K. Mueller, *Identifying sets of favorable projections for few-view low-dose cone-beam CT scanning*, in: *11th International meeting on fully three-dimensional image reconstruction in radiology and nuclear medicine*, 2011, pp. 314–317.
- [31] T. Buzug, *Computed Tomography: From Photon Statistics to Modern Cone-Beam CT*, Springer, Berlin Heidelberg, Berlin, Heidelberg, 2008.
- [32] G. Herl, J. Hiller, A. Maier, *Scanning trajectory optimisation using a quantitative Tuybased local quality estimation for robot-based X-ray computed tomography*, *Nondestruct. Test. Eval.* 35 (2020) 287–303.
- [33] C. Bellon, A. Deresch, C. Gollwitzer, G.-R. Jaenisch, *Radiographic simulator aRTist: version 2*, : 18th World Conf. Nondestruct. Test. (2012) 16–20.
- [34] Deutsches Institut für Normung (DIN), *Europäische Normungsorganisation (EN), Internationale Organisation für Normung, Zerstörungsfreie Prüfung – Non-destructive testing - Radiation methods for computed tomography - Part 2: Principles, equipment and samples (ISO 15708-2:2017); German version EN ISO 15708-2:2019.*
- [35] J. Müller, G. Herl, T. Schromm, P. Jahnke, A. Maier, *Task-specific View Selection for 2D X-ray Inspection of Large Objects with Robotic CT Systems* (2024).
- [36] R. Swinbank, R.J. Purser, *Fibonacci Grids*, Preprints of the 13th Conference on Numerical Weather Prediction (1999) 125–128.
- [37] J. Kumar, F. Chen, D. Doermann, *Sharpness estimation for document and scene images*, in: *Proceedings of the 21st International Conference on Pattern Recognition (ICPR2012)*, 2012, pp. 3292–3295.
- [38] D. Sadykova, A.P. James, *Quality assessment metrics for edge detection and edge-aware filtering: A tutorial review*, in: *2017 International Conference on Advances in Computing, Communications and Informatics (ICACCI)*, 2017, pp. 2366–2369.